Plasma Adaptive Optics Evaluation Using Two-Wavelength Heterodyne Interferometry

Brian W. Neiswander[1] and Eric Matlis[2]
University of Notre Dame, Notre Dame, Indiana, 46556

Thomas C. Corke[3]
University of Notre Dame, Notre Dame, IN 46556

The third part of a research program that investigates the possibility of using low-temperature ionized air (plasma) for adaptive optics in an airborne laser directed energy system is presented. It involves a novel optical measurement method that consisted of a dual wavelength Michaelson interferometer that included a micro-actuated mirror to allow heterodyne operation. The heterodyne interferometry was an important element in extracting the individual effects of electrons and heavy particles on the optical properties of the plasma. The plasma was generated in a hollow glass cylinder that was sealed at both ends by optical glass. It utilized an AC voltage source whose amplitude was modulated in order to produce side-band phase modulations for heterodyne analysis. A robust demodulation scheme was developed to extract the modulated interferometric phase shifts to reveal the temporal evolution of electron and heavy particle densities within the plasma. The contributions of electron and heavy particle densities to the plasma optical path difference (OPD), which is a measure of optical control, was calculated. Based on a aero-optic standard 1 μm wavelength, for the conditions examined in the experiment with air, the combined contributions yielded an $OPD = -300$ nm, which is two-times larger than nominal OPD values in aero-optic applications.

---

[1] Postdoctoral Research Associate, Department of Aerospace and Mechanical Engineering, AIAA Member
[2] Research Assistant Professor, Department of Aerospace and Mechanical Engineering, AIAA Member
[3] Clark Chair Professor, Department of Aerospace and Mechanical Engineering, AIAA Fellow

I. Introduction

Directed energy and laser-communications technology in airborne applications rely on the use of adaptive optics (AO) systems for sufficient energy delivery and data transfer[1]. This is necessary to compensate for time-dependent density gradients caused by compressible turbulent boundary layers and wakes that form on or near the aircraft. Aberrations are characterized in terms of an optical path difference (OPD), which is the physical length to which the wavefront is distorted. Typical root-mean-square OPD values in aero-optic applications range from 25 to 150 nm[2]. Such levels of OPDs generated in the near-field significantly reduce the intensity of a beam as it propagates into the far-field[2–4].

One approach towards mitigating this problem is to employ an on-board adaptive optics (AO) system to perform real-time OPD corrections and restore planar wavefronts. Such an AO system is typically comprised of a wavefront sensor to measure the OPD, a controller to process and prescribe corrections, and an active wavefront control device to correct for aberrations. The control device is typically a deformable mirror which is a segmented or continuous reflective surface that spatially distorts itself to reflect back planar wavefronts. Deformable mirrors are electro-mechanical devices that have some inertial limitations. Correction rates typically range from hundreds of Hertz to a few kilo-Hertz. Mechanical deformable mirrors are generally delicate and eventually fail due to material fatigue. Therefore there is a desire to develop more robust wavefront control devices that also might have improved frequency response.

Under appropriate conditions, the index of refraction of a plasma varies linearly with its electron density[5]. Since the plasma electron density can be varied through its applied electric field, this approach can provide a method for dynamically controlling the index of refraction. If the plasma is confined within a volume, it is possible to effectively created a “plasma lens" with a variable index of refraction. A conceptual representation is shown in Figure1. The frequency response of such a “plasma lens" is only limited by the recombination time of electrons and ions, and likely could be in the range of hundreds of kilohertz[6].

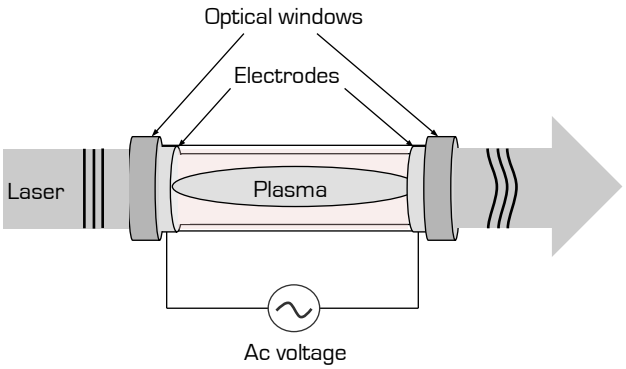

Fig. 1 Conceptual representation of a plasma adaptive optics (PAO) lens.

In a previous proof-of-concept by the authors[7] interferometry[8] was used to characterize the OPD produced by a cylindrical PAO lens consisting of plasma confined in a 15.2 cm long by 1.9 cm outside-diameter hollow thin-walled glass cylinder. Electrode bands encircled the outside of the glass cylinder. The electrodes were connected to a variable high-voltage AC source that produced a classic double-dielectric discharge plasma inside the cylinder. The scale of the setup provided a long plasma extent for the laser to pass through, and OPD values greater than 100 nm were achieved[7]. Contours levels of OPD at the exit of the cylindrical PAO lens showed good radial uniformity, particularly at the higher voltages. An example of these OPD contours is shown in Figure 2

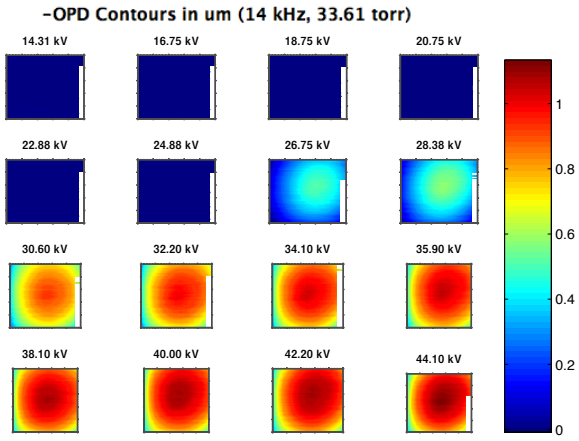

Fig. 2 Radial distribution of OPD for different AC voltages in the authors proof-of-concept cylindrical PAO lens.[7]

The radial uniformity of the OPD was further investigated by the authors[9]. This led to a

theoretical criterion for the wrapped electrode diameter (same as the glass cylinder outside diameter), D, to axial electrode spacing, d, to ensure that the plasma formed uniformly along the axial centerline of the PAO lens. The critical ratio was $d/D = 1.22$, which was validated by experiment[9].

Our previous work[7] used single wavelength interferometry to measure electron density, using the assumption that the heavy particle contribution to refractive index was negligible[7]. Under sufficiently strong electric field however, the ionized gas generates two groups of particles: free electrons and heavy particles. The latter is a generic term that refers to neutral, metastable, and ionic species inside the gas. Each of these particle groups independently affect the optical characteristics of the plasma. The optical contributions from electrons and heavy particles are described in terms of the plasma index of refraction, N, given as[10]

$$N - 1 = -\frac{q^2 \lambda^2 n_e}{8\pi^2 \epsilon_0 c^2 m} + \left(A + \frac{B}{\lambda^2}\right) \frac{n_h}{n_{h0}}, \tag{1}$$

where q is electron charge, λ is the wavelength of light probing the plasma, n_e is the plasma electron density, ϵ_0 is the free space permittivity, c is the speed of light, m is electron mass, A and B are a gas constants, n_h is the heavy particle density, and n_{h0} is the heavy particle density at a reference temperature and pressure. The first term on the right hand side of Equation 1 represents the contribution of free-electrons to the change in the refractive index. The second term on the right hand side of Equation 1 represents the the effect of the heavy particle on the plasma refractive index. Both are functions of their respective number densities in the plasma.

The heavy particles inside the plasma are nearly ten orders of magnitude more massive than the free electrons. Therefore it follows that these particles also have very different time scales. The lighter electrons are able to react to changes in the electric field almost instantaneously in comparison to the heavy particles, which feature a more significant response lag[11]. For the purpose of aero-optics, the free electron contribution is more desirable due it its higher frequency response potential.

The determination of plasma electron density from refractive index measurements requires some assumptions about the heavy particle contribution. One common technique involves time-resolved interferometric measurements, which exploit the different time-scales between electrons and heavy particles[12, 13]. Multi-wavelength interferometry is another common approach, in which mea-

surements at two or more distinct probing wavelengths allows the formation of a linear system of equations (based on Equation 1) that can be solved to determine the respective particle densities[14].

A. Objective

The object of the present work was to determine the individual effects of free electrons and heavy particles on the OPD produced by the PAO lens configuration. To achieve this, a heterodyne two-wavelength interferometry[15] will be utilized. This was an improvement over our previously used[7] single wavelength interferometry, or standard non-heterodyne dual-wavelength interferometry generally used for this purpose[16].

The determination of the change in electron and heavy particle densities will depend on accurately measuring the phase change reflected in the shift in the interferometer fringe patterns. The issue is that even the smallest imperfection in the physical setup such as air currents or vibration, could change the absolute position of the fringes, producing an error in the phase measurement. Furthermore, as pointed out by Wolfe at al.[17], if the phase shift, Φ, were close π, the sensitivity which is proportional to $\sin(\Phi)$, is very low. To overcome this, a phase-modulated self-heterodyne interferometer is implemented. In general a phase modulator is described by the relation $y(t) = A_c sin(\omega_c t + m(t) + \phi_c)$, where A_c is the carrier amplitude, ω_c the frequency of the carrier, and $m(t)$ is the information to be transmitted; in this case the plasma-induced phase shift. This is accomplished by including a moving mirror in one leg as the heterodyne source to create the carrier signal. The plasma waveform is then modulated with a sinusoidal envelope to generate side-bands. The phase information contained in the side-bands can then be retreaved through a demodulation scheme. This approach will make the sensitivity of the resulting phase measurement independent of the instantaneous phase, and unaffected by fluctuations in the physical setup.

Details of the design of the two-wavelength heterodyne interferometer are presented. In addition, the step-by-step analysis leading to measurements of the electron and heavy particle densities is shown. The resulting measurements are then used to estimate the OPD performance at the aero-optic standard 1 μm probing wavelength.

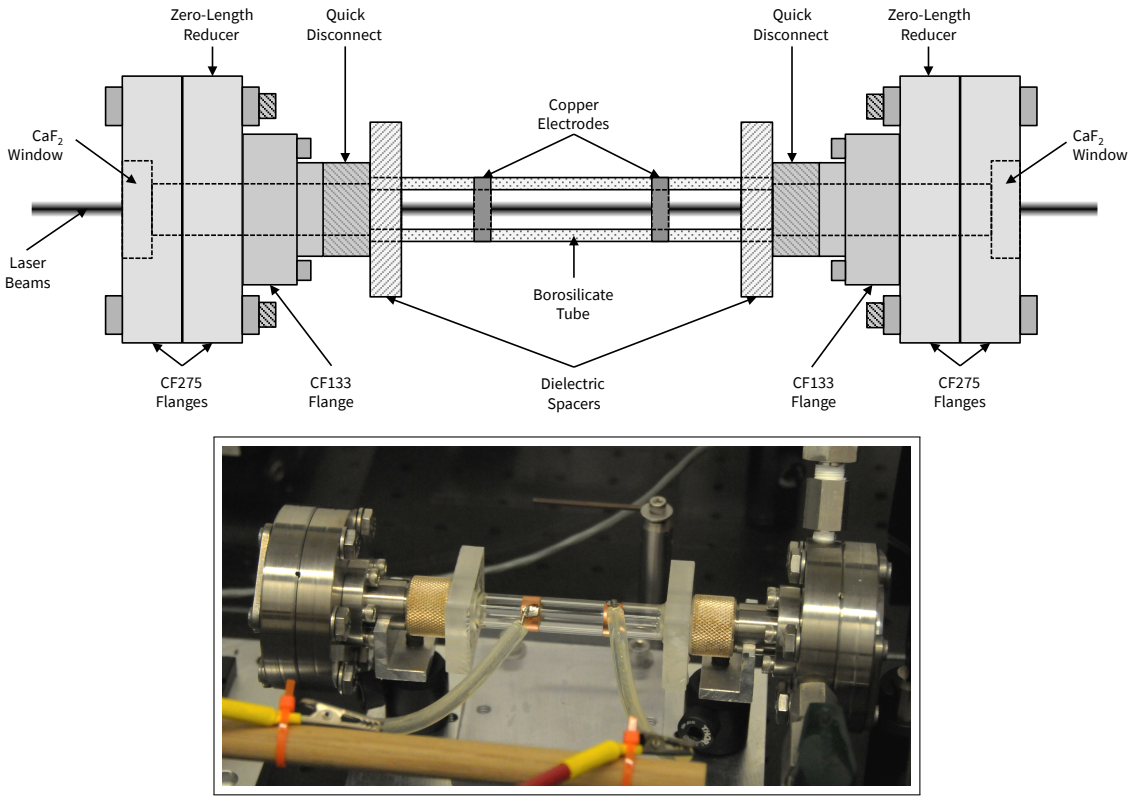

Fig. 3 Schematic (top) and photograph of PAO setup.

II. Experimental Setup and Procedure

A. Plasma Chamber

As in our previous work[7, 9], a stable low-temperature plasma was generated in a hollow glass cylinder PAO geometry that was conceptualized in Figure 1. The exact setup used in the present experiments is shown in Figure 3. The glass cylinder consisted of a borosilicate tube with a 1.2 cm outer diameter and 1.6 mm wall thickness. Each end of the glass tube was sealed through an assembly that consisted of a 3.38 cm diameter quick-disconnect adapter, CF flange and CF zero-length reducer. A 2.5 cm diameter calcium-fluoride (CaF_2) window on each end of the assembly allowed optical access for the laser beams to pass through the axial centerline of the tube.

A plug valve was mounted to one of the zero-length reducers and connected to a pressure manifold. Pressure inside the borosilicate tube was reduced using a two-stage vacuum pump and monitored with a vacuum pressure transducer. Once a desired pressure was reached, the plug valve was closed and the pump was turned off to avoid vibrations. The plasma chamber was leak-tested

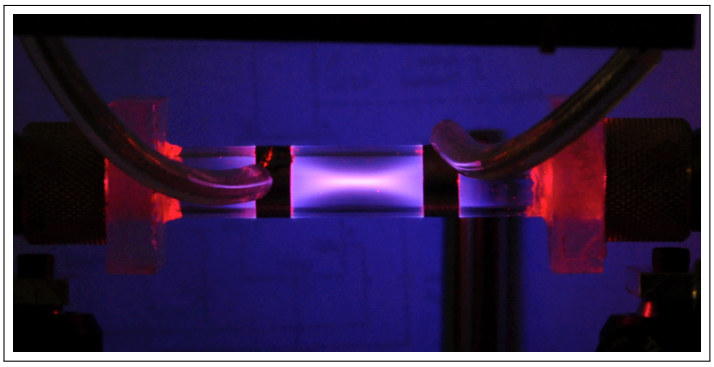

Fig. 4 Photograph of plasma forming along the axial centerline of the PAO glass tube.

using a Varian 959 Macrotorr Helium Leak Detector and shown to have a leak rate of less than 2×10^{-8} cm^3/s.

Two 6.4 mm-wide copper tape electrodes were wrapped around the outside of the borosilicate tube. The electrodes were separated by a gap distance of 23.9 mm, making the ratio of electrode gap distance, d, to electrode diameter, D, equal to 1.88. This conforms to the ratio required to cause plasma to form in the axial centerline of the tube [9]. This was validated in the photograph of the plasma formation with the present setup shown in Figure 4.

The electrodes that encircled the borosilicate tube were powered by an AC voltage source made up of a variable frequency function generator, audio amplifier to increase the current, and a voltage step-up transformer. The AC voltage was measured using a high-voltage probe. The current was measured with a wide-band inductive current monitor. The voltage and current time series were monitored and recorded using a digital oscilloscope. A digital camera was located to the side of the plasma chamber to acquire images of the plasma during the experiment operation.

The AC voltage source to the plasma was amplitude modulated with a sinusoidal envelope, as depicted in Figure 5. The purpose of the amplitude modulation was to produce sideband frequency components that were used with the heterodyne analysis. The maximum peak-to-peak voltage inside the envelope was 42 kV. During each modulation cycle, when the voltage reached the initiation level, plasma formed. From that point as the voltage followed the amplitude envelope, the electric field strength and presumably the plasma ionization level followed in a similar manner. When the voltage fell below that needed to sustain the plasma, it extinguished. In addition to providing temporal

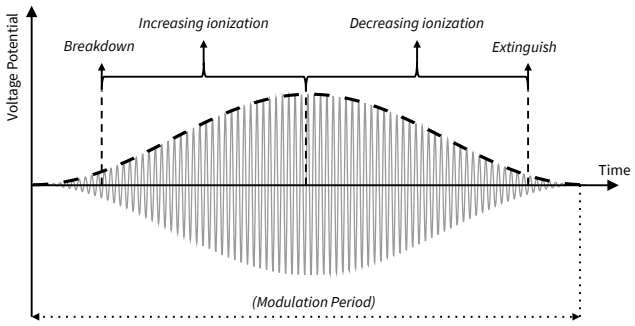

Fig. 5 Schematic of the AC voltage amplitude modulation waveform used for powering the plasma.

information for the heterodyne post-analysis, it also provided the plasma optical property for a large, continuous range of voltage potentials. One further point about the AC source amplitude modulation was that only the *dynamic effects* were considered, which removed any slow varying changes in the gas conditions during the short run times.

During the experiments three frequencies were used to generate the plasma: 2, 3 and 4 kHz. These frequencies are high enough to ensure that the plasma is considered *quasi-steady* relative to the thermal diffusion time constant and the dynamics of the heterodyne process. To generate the side-bands necessary for the phase modulation scheme, the plasma envelope was modulated at a frequency that is not a subharmonic of the AC generation. Three modulation frequencies were considered: 27, 37, and 47 Hz. The combination resulted in from 42 to 74 carrier frequency cycles per modulation period. A total of 100 contiguous modulation cycles were acquired, which corresponded to a 2.1 to 3.7 second run time.

B. Two-Wavelength Heterodyne Michelson Interferometer

A two-wavelength Michelson heterodyne interferometer was used to measure the relative phase differences produced by the PAO powered by the amplitude modulated AC voltage. This utilized a visible 633 nm helium neon laser and an infrared 3.39 μm helium neon laser. A schematic of the interferometer setup is shown in Figure 6.

The heterodyne interferometer was constructed on an optical table with air-spring vibration isolation legs to reduce noise from any external vibrations. Both lasers were aligned onto the same

beam path using an anti-reflective coated window. The interferometer included a 5.08 cm diameter germanium-coated potassium bromide (KBr) beamsplitter and two 1.27 cm diameter mirrors. The beamsplitter split the two laser beams into two paths: one through the plasma chamber (plasma arm) and one through air (reference arm). A mirror placed at the end of each arm reflected each beam back towards the beamsplitter. The distance between the beamsplitter and mirror was 35.6 cm. The beamsplitter material was hygroscopic and required dehumidifiers to maintain a relative humidity level below 40%. The entire interferometer was placed inside an acrylic enclosure to eliminate possible disturbances produced by air currents within the laboratory space.

The beam diameters passing through the PAO were 1.23 mm for the visible laser and 2.02 mm for the infrared laser. Based on the OPD contours from our previous work[7] that were shown in Figure 2 and that overlap the conditions in the present experiment, these beams easily fit within the radially uniform OPD region along the axial centerline of the PAO.

The heterodyne capability was incorporated through a moving mirror that was located in the plasma arm of the interferometer. The mirror was mounted on a linear stage driven by a piezoelectric actuator (Nanomotion FB050-020-10N4). The linear stage featured a 10 nm optical encoder and had a maximum travel distance of up to 20 mm. The linear stage was operated to translate the mirror parallel to the beam path, at a constant velocity away from the beamsplitter. Therefore as the mirror moved, the path length of the plasma arm increased, producing a change in the optical path length between the interferometer plasma and reference arms.

The laser beams passing through the plasma and reference arms were ultimately recombined to produce visible and infrared interferograms. The interferograms were focused using an off-axis parabolic mirror and split into visible and infrared components using an anti-reflective coated window. The visible interferogram was focused onto a silicon photoconductive detector, and the infrared interferogram was focused onto a lead selenide photoconductive detector. The analog outputs from the two photodetectors were digitally sampled using a 16-bit data acquisition (DAQ) system connected to a digital computer.

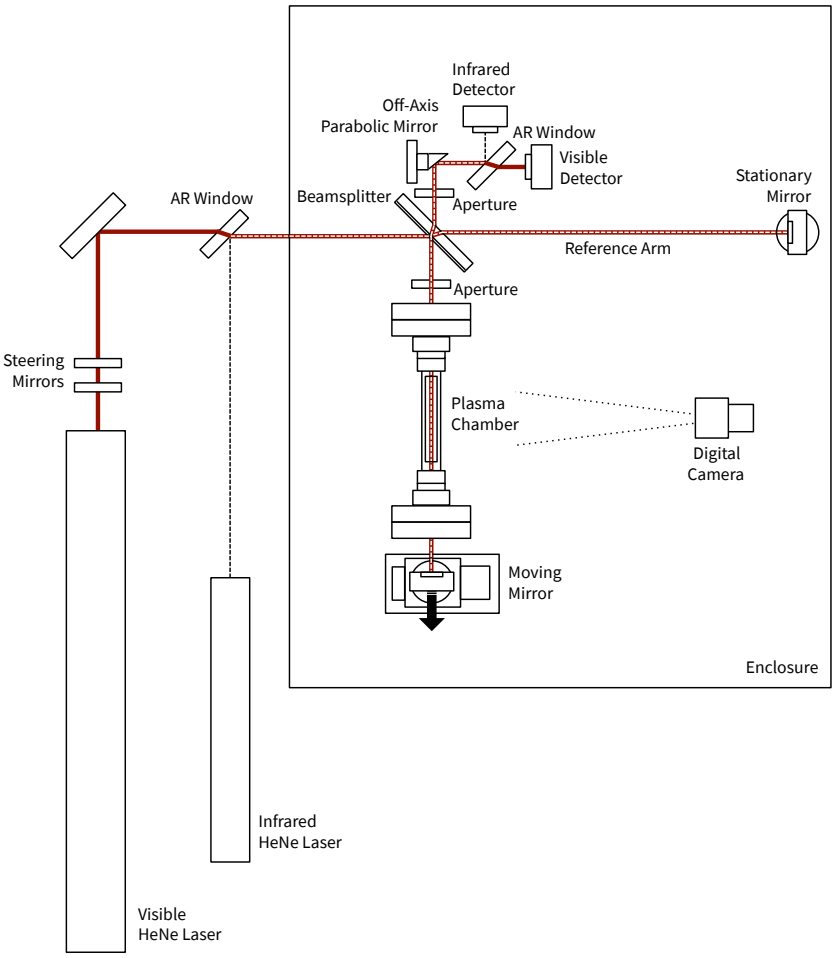

Fig. 6 Schematic of the two-wavelength heterodyne Michelson interferometer used to simultaneously measure electron and heavy particle densities in PAO system.

C. Experimental Procedure and Data Acquisition

A diagram of the experimental components, sensors, and data acquisition devices used in the experiments is shown in Figure 7. As was depicted in Figure 5, the function generator produced an amplitude-modulated carrier frequency voltage time series that was amplified to the level needed to ionize the air inside the PAO over a portion of the modulated amplitude cycle. The time-resolved voltage and current to the PAO was monitored with voltage and current probes and displayed on an oscilloscope. The analog outputs from the visible and infrared photoconductive detectors was acquired by a digital data acquisition system and stored on a digital computer for later post processing. The oscilloscope and digital data acquisition were triggered in phase with the amplitude modulation frequency. This allowed for the ensemble averaging of the photoconductive detectors

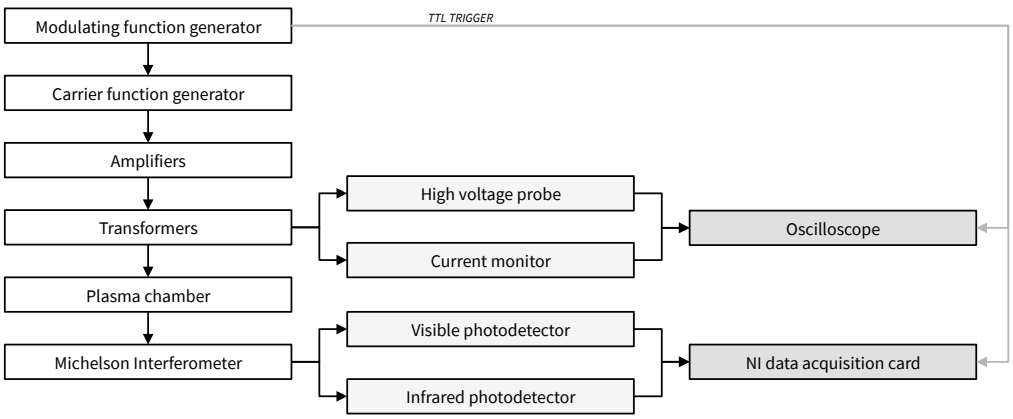

Fig. 7 Diagram of the experimental components, sensors, and data acquisition devices used in operating the PAO to acquire visible and infrared interferograms from the two-wavelength Michaelson heterodyne interferometer.

outputs. The total sampling time for each data run was 100 AC voltage modulation cycles which corresponded to from 2.1 to 3.7 seconds.

Special care was taken to maximize the signal-to-noise ratio of the photoconductive detectors outputs. The alignment of the interferometer was adjusted using the reference arm mirror to produce optimal fringe contrast in both the visible and infrared interferograms. The entire optical system was placed in an enclosure to eliminate any effects of room air currents. In addition, the lights in the room were turned off during data sessions to prevent any contamination of the visible photoconductive detectors.

A summary of the experimental conditions is given in Table 1. The gas inside the PAO glass cylinder was air. The air pressure ranged from 20 to 60 Torr. In this range of pressures, the plasma formation was steady. This was documented both visibly and in the photoconductive detectors output. At higher pressures above 60 Torr, the plasma formation became unsteady. The order of the carrier and voltage amplitude modulation frequency combinations was randomized to minimize any possible hysteresis effects.

A data acquisition run consisted of 100 contiguous modulation cycles of the AC voltage for

Table 1 Summary of experimental conditions.

Experimental Parameter	Value	Unit
Gas	Air	
Pressure	20-60	Torr
Plasma AC frequency	2, 3, 4	kHz
Plasma AC voltage modulation frequency	27, 37, 47	Hz
Moving mirror velocity	300	μm/s
Visible laser wavelength	0.6328	μm
Infrared laser wavelength	3.392	μm
DAQ sampling frequency	125	kHz
Oscilloscope sampling frequency	20	MHz

a given carrier frequency, which corresponded to a 2.1 to 3.7 second run time. The air pressure inside the PAO was monitored before and after each data acquisition run to insure the operating condition, and to note any changes following the run. The moving mirror piezoelectric stage was set to translate at a velocity of 300 μm/s. The time for the motion of the mirror to reach its travel limit (20mm) was well within the data acquisition run time. Its motion was started before AC voltage modulation was initiated. The AC modulating function generator was then manually triggered to begin the plasma generation, which also triggered the acquisition of the voltage and current supplied to the PAO plasma, and the acquisition of the visible and infrared photodetector voltage time series.

Following each data acquisition run, the air in the PAO glass tube was completely vented to the lab. In this way there was always a fresh air composition without residual effects on the air in the PAO from the previous data acquisition run.

III. Analysis

With each acquisition run corresponding to a fixed gas pressure, AC frequency, and AC voltage modulation frequency, the visible and infrared interferograms from the heterodyne interferometer were sampled with their respective photodetectors. The photodetector outputs included contributions from three major components: (1) the carrier signal due to the moving mirror, (2) side-band

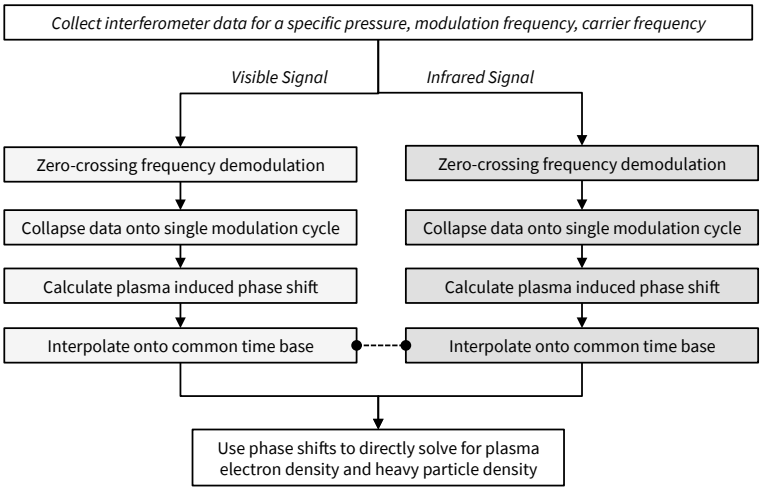

Fig. 8 Schematic of the 5-step data processing used to determine the PAO electron and heavy particle densities from the heterodyne interferometer data.

generation due to the plasma AC amplitude modulation and (3) noise due to mirror velocity fluctuations, vibrations, acoustics, and electronic noise.

The post-processing of each photodetector time series consisted of five steps: (1) zero-crossing frequency demodulation to remove the carrier signal produced by the moving mirror, (2) phase-locking to reduce the effects of noise components, (3) the calculation of the PAO imparted phase shift, (4) an interpolation to a common time base, and (5) the calculation of the PAO electron and heavy particle densities. A schematic of this 5-step process is shown in Figure 8. The following sections describe these steps in greater detail.

A. Zero-Crossing Frequency Demodulation and Plasma Induced Phase Shift

As previously discussed, a moving mirror was introduced into one leg of the interferometer in order to overcome difficulties in accurately resolving the phase shift in the interference fringes that resulted from the PAO. The issue was that even the smallest imperfection in the physical setup could change the absolute position of the fringe, adding to the measurement uncertainty. In addition, the sensitivity near π phase shifts is very low. This was overcome by using a moving mirror to generate a carrier that was phase-modulated by a sinusoidally-varying plasma amplitude envelope.

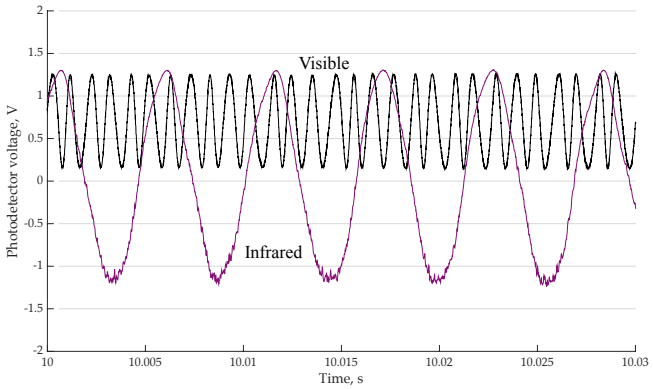

Fig. 9 Sample photodetector output time series illustrating the two different carrier frequencies produced by the moving mirror for the visible and infrared components.

The carrier frequencies, f_c, were a function of the mirror velocity, V_m and the probing laser wavelength, λ, whereby $f_c = 2V_m/\lambda$. With the $V_m = 300$ μm/s used in the experiments, this resulted in carrier frequencies of 948.2 Hz and 176.9 Hz for the respective visible and infrared photodetector outputs. This is illustrated in the sample photodetector output time series shown in Figure 9 where there is an approximately 5:1 ratio between the periods associated with the visible and infrared sources.

A zero-crossing frequency demodulation scheme was developed to remove the carrier frequency component from the photodetector output time series. For this, the time series were first low-pass filtered to remove any high-frequency noise that might affect the zero-crossing detection. This utilized a second-order Butterworth filter with a corner frequency of $10f_m$. It was verified that the filtering did not introduce any phase shift in the time series. The time between zero crossings in the filtered time series were then determined and used to construct frequency time series, $f(t)$, for the respective photodetector outputs.

The constructed frequency time series, $f(t)$, included the mean carrier frequency, and any time-varying phase changes[8], namely,

$$f = \overline{f} + \frac{d\Phi}{dt}, \tag{2}$$

where the bar denotes the time-averaged value. Our interest was in the instantaneous phase, $\Phi(t)$.

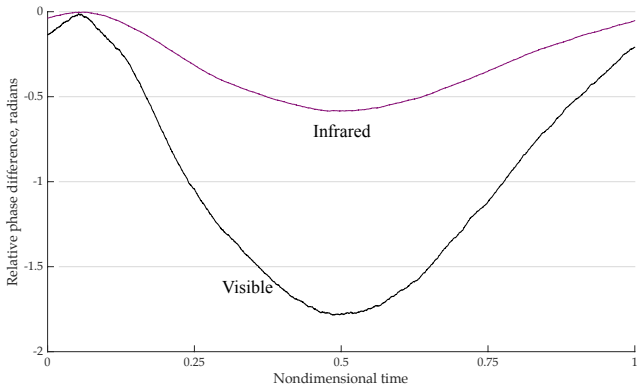

Fig. 10 Sample plasma induced phase shifts $\Delta\Phi_V(t)$ and $\Delta\Phi_I(t)$ for one of the experimental cases.

This was determined using a trapezoidal approximation for the integral of $f - \overline{f}$, namely

$$\Phi = \{\Phi_i\} = \frac{1}{2}\sum_{j=1}^{i}\left(t_{j+1} - t_j\right)\left(f_{j+1} + f_j - \overline{f}\right) \qquad \text{for } i = 1, 2, 3, ..., N-2. \tag{3}$$

Evaluating Equation 3 for the visible and infrared photodetector signals gave the respective plasma induced phase shifts $\Delta\Phi_V$ and $\Delta\Phi_I$. Note that the zero-crossing demodulation scheme produced a multi-rate signal because samples are only logged at zero-crossing events, which were different for each wavelength. To mitigate this, the signals $\Delta\Phi_V$ and $\Delta\Phi_I$ were linearly interpolated to share a common time base.

The amplitude modulation of the PAO voltage represented a repetition of the plasma formation that was used to obtain ensemble averages of the induced phase shifts during an amplitude modulation cycle. Figure 10 shows typical plasma induced phase shift profiles $\Delta\Phi_V(t)$ and $\Delta\Phi_I(t)$ for one amplitude modulation cycle in one of the experimental cases.

B. Determination of Electron and Heavy Particle Density

The ensemble phase shifts $\Delta\Phi_V(t)$ and $\Delta\Phi_I(t)$ were subsequently used to determine the electron and heavy particle densities in the PAO for the various operating conditions. The plasma index of refraction, N, given by Equation 1), is related to the plasma induced phase shift as

$$\Delta\Phi = \frac{2\pi}{\lambda}\left(\int_0^{2L} N_{on}(l)dl - \int_0^{2L} N_{off}(l)dl\right) = \frac{2\pi 2L}{\lambda}\left(-\frac{q^2\lambda^2\Delta n_e}{8\pi^2\epsilon_0 c^2 m} + \left(A + \frac{B}{\lambda^2}\right)\frac{\Delta n_h}{n_{h0}}\right). \tag{4}$$

The interferometer in this experiment featured two probing frequency wavelengths. Therefore, Equation 4 was written for each wavelength, namely

$$\Delta\Phi_V = \alpha(\lambda_V)\Delta n_e + \beta(\lambda_V)\Delta n_h, \tag{5}$$

and

$$\Delta\Phi_I = \alpha(\lambda_I)\Delta n_e + \beta(\lambda_I)\Delta n_h \tag{6}$$

where generally (without subscripts)

$$\alpha(\lambda) = \frac{-Lq^2\lambda}{2\pi\epsilon_0 c^2 m}, \tag{7}$$

and

$$\beta(\lambda) = \left(A + \frac{B}{\lambda^2}\right)\frac{4\pi L}{\lambda\ n_{h0}}. \tag{8}$$

Equations 5 and 6 feature two unknowns: the change in electron density, Δn_e, and the change in heavy particle density, Δn_h. With substitution and rearranging of terms, the following expressions for Δn_e and Δn_h as functions of the respective $\Delta\Phi$ are obtained, namely

$$\Delta n_e = \frac{\beta(\lambda_I)\ \Delta\Phi_V - \beta(\lambda_V)\ \Delta\Phi_I}{\alpha(\lambda_V)\ \beta(\lambda_I) - \alpha(\lambda_I)\ \beta(\lambda_V)} \tag{9}$$

and

$$\Delta n_h = \frac{\alpha(\lambda_I)\ \Delta\Phi_V - \alpha(\lambda_V)\ \Delta\Phi_I}{\beta(\lambda_V)\ \alpha(\lambda_I) - \beta(\lambda_I)\ \alpha(\lambda_V)}. \tag{10}$$

Based on Equations 7, 8, 9, and 10, and with two probing laser wavelengths, it was then possible to determine the change in electron and heavy particle densities within the PAO between it being on and off. This information could then be related to the OPD and more specifically to the relative contributions of electrons and heavy particles to the OPD.

IV. Experimental Results and Discussion

Experiments were conducted to parametrically investigate the dependence of the electron and heavy particle densities on input parameters consisting of the PAO gas pressure, AC voltage (carrier) frequency, and AC amplitude modulation frequency. The data consisted of the visible and infrared

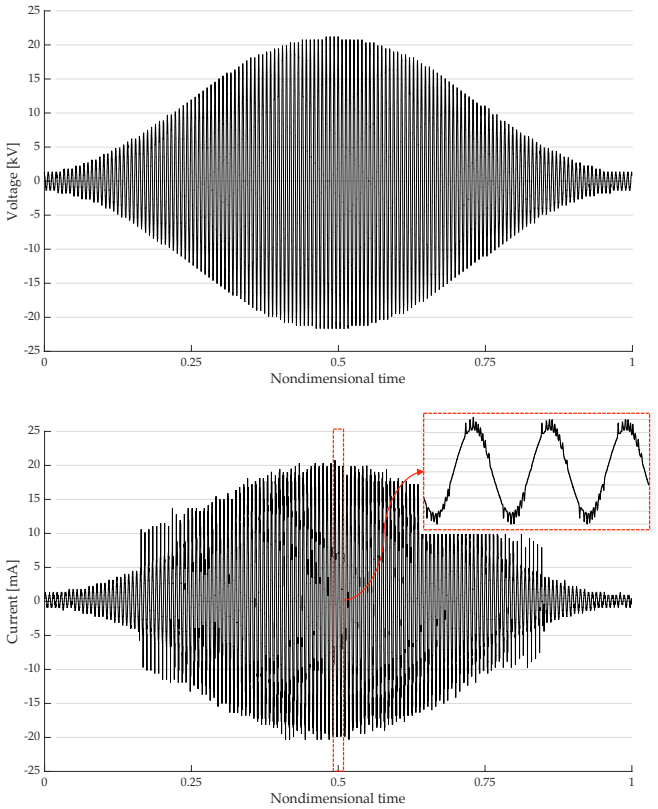

Fig. 11 Sample voltage and current time series during an amplitude modulation cycle. Inset is an enlarged view illustrating small current fluctuations indicative of plasma formation.

photodetector voltage time series that were processed to determine fringe phase shifts that could ultimately be used to determine the changes in electron and heavy particle densities in the PAO.

An example of the input voltage time series and the resulting current time series during an amplitude modulation cycle is shown in Figure 11. The sharp changes in the current at nondimensional times of approximately 0.2 and 0.8 respectively correspond to the locations where the voltage was large enough to initiate the plasma and where it fell below that where the plasma could no longer be maintained. This is further evident in the computed power supplied to the PAO shown in Figure 12. This includes all of the experimental combinations of the input AC frequencies and air pressures used with the PAO. The power levels asymptote to near zero values when the air in the PAO is not ionized. The portion of the amplitude modulation cycle where this occurred was relatively insensitive to the input conditions used in the experiments.

An example of the changes in the electron and heavy particle densities during an amplitude

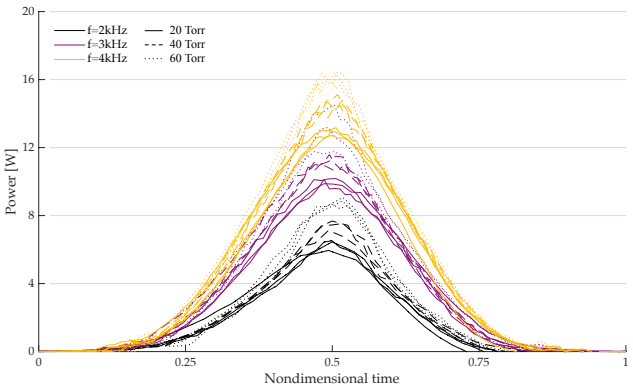

Fig. 12 Power time series during an amplitude modulation cycle for the combinations of the input AC frequencies and air pressures used with the PAO.

modulation cycle for the range of PAO gas pressures is shown in Figure 13. For this, the AC and amplitude modulation frequencies were fixed at 4 kHz and 37 Hz, respectively. Note that the ordinate for the plot of the *change* in heavy particle density is *negative* values.

Figure 13 illustrates a number of important observations. The first was that the magnitude of the change (plasma on minus plasma off) in the electron density was three-orders of magnitude smaller than that for the heavy particles. The $\mathcal{O}(10^{14})$ cm^{-3} change in electron density was consistent with the diffusive nature of the PAO plasma, and the power levels supplied. The electron density increased with increasing PAO air pressure which was consistent with a decreasing air mean-free-path at higher pressures. The trend with the heavy particle density was opposite to that of the electron density. That is, it decreased with increasing air pressure.

The effect of the AC voltage frequency on the changes in the electron and heavy particle densities during an amplitude modulation cycle at a fixed PAO air pressure is shown in Figure 14. In this case, the air pressure was the highest investigated (60 Torr) and the amplitude modulation frequency was again 37 Hz. These plots indicate that the electron density increased with increasing AC frequency. This was consistent with the higher AC power supplied per amplitude modulation cycle. The trend with the heavy particle density was again opposite to that of the electron density. That is, it decreased with increasing AC frequency.

A final important feature involves the observed small differences in the change in the heavy

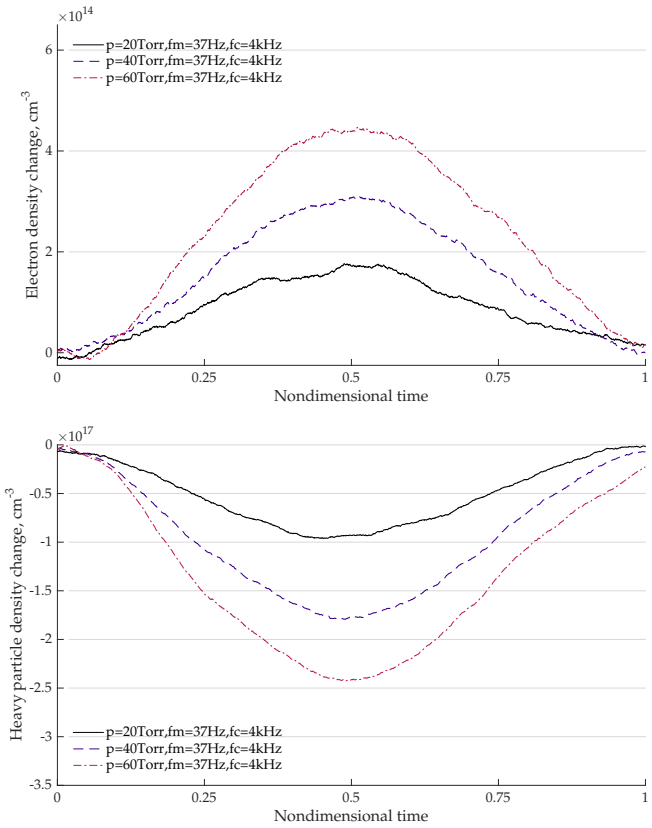

Fig. 13 Example of the change in the electron and heavy particle densities during an amplitude modulation cycle for the range of PAO gas pressures. AC and amplitude modulation frequencies were fixed at 4 kHz and 37 Hz, respectively.

particle density at the end of the amplitude modulation cycle compared with that at the beginning. Such a difference, particularly with the heavy particle density might be attributed to a number of factors, namely a steady change in the air chemistry, or a steady change in the gas pressure or temperature. In the two cases in Figures 13 and 14, the period of each amplitude modulation cycle was 27 ms, and the total duration of the measurements (100 modulation cycles) was 2.7 seconds. The results shown in Figure 13 corresponded to experimental conditions with the highest AC frequency, which resulted in the highest power levels to the PAO. In this case, the difference in heavy particle density between the beginning and end of the cycle was only noteable at the highest pressure. For the results in Figure 14 which were all at a pressure of 60 Torr, the difference between the beginning and end of the cycle was again only noteable at the 4 kHz AC frequency. Therefore whatever the cause, it was only noteable for the single case of the highest AC frequency and gas

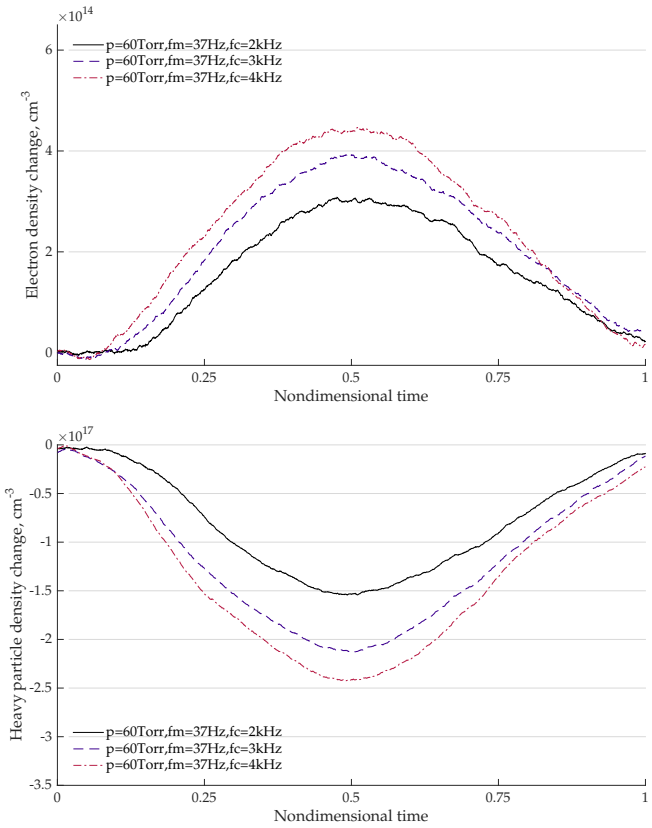

Fig. 14 Example of the change in the electron and heavy particle densities during an amplitude modulation cycle for the range of AC frequencies. PAO gas pressure and amplitude modulation frequency were fixed at 60 Torr and 37 Hz, respectively.

pressure. Therefore at minimum in all the other cases, the majority of the observed changes in heavy particle and electron densities are associated with the dynamics of the plasma modulation. With regard to the 4 kHz, 60 Torr condition, the small decrease in the heavy particle density at the end of the amplitude modulation cycle would be the consistant with a small increase in the mean temperature of the air. However, that difference only affects the one case, and is small compared to the peak change in the heavy particle density which is ultimately used to evaluate the effectiveness of the PAO.

The results of all the cases were compiled into two plots documenting the maximum change in electron and heavy particle densities as a function of the PAO air pressure. These plots are shown in Figures 15 and 16. Again we note that the ordinate for change in heavy particle density is *negative* values. The dashed lines are linear least-square error fits of the densities as a function of pressure.

As observed in the previous figures, conditions that increase the electron density result in a reduction in the heavy particle density, with the largest positive change in electron density corresponding to the largest negative change in the heavy particle density. For the most part, the change in *heavy particle density* with pressure is reasonably represented by the linear curve fit. However for the electron density, the results are mixed. In particular, the linear change in electron density with pressure is a reasonable representation at the lower AC voltage frequencies, that resulted in the lowest electron densities. At the higher AC frequencies (e.g. 4 kHz), producing higher electron densities, the variation in electron density with air pressure is decidedly *not linear*, appearing more quadratic. The results of these experiments were subsequently used to estimate the PAO for an aero-optics standard 1 μm probing wavelength.

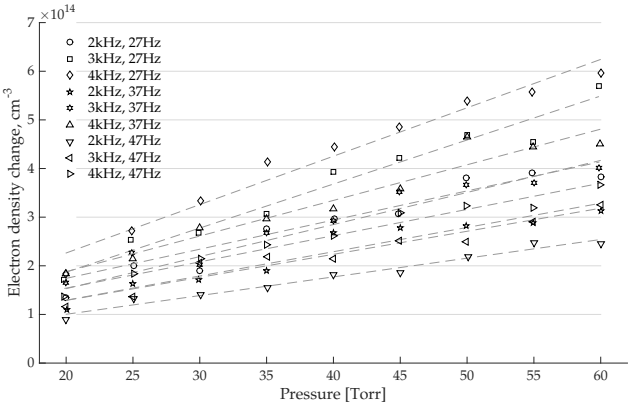

Fig. 15 PAO change in electron density as a function of air pressure for different AC voltage and amplitude modulation frequencies.

A. Estimation of Aero-Optic Performance

The object of this section was to utilize the experimental results of the change in electron and heavy particle densities documented in the previous figures to determine the PAO OPD for a probing wavelength of 1 μm. The amplitude modulation that was required for the heterodyne post-processing would not be used for general PAO operation. Therefore it was necessary for the PAO performance prediction to extrapolate the trends for the electron and heavy particle densities to that for a zero modulation frequency. Figures 17 and 18 show the trend in electron and heavy particle densities

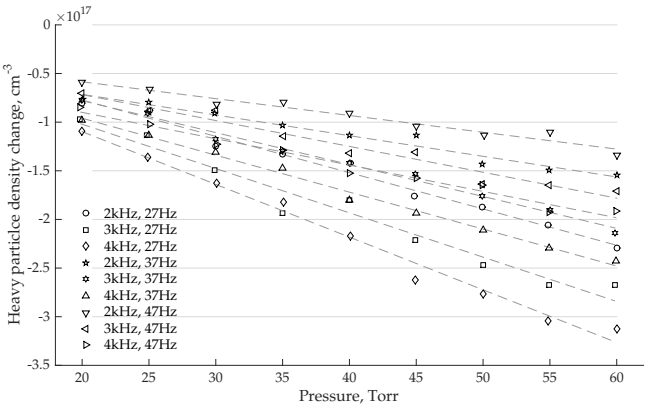

Fig. 16 PAO change in heavy particle density as a function of air pressure for different AC voltage and amplitude modulation frequencies.

as a function of the amplitude modulation frequency at the condition that produced the highest electron density, an air pressure of 60 Torr and an AC voltage frequency of 4 kHz. Again following our convention, the ordinate for change in heavy particle density is *negative* values. The dashed line corresponds to a linear curve fit of the data. The linear fit follows the trends reasonably well. It was therefore used to extrapolate to determine the change in the electron and heavy particle densities for the 60 Torr and 4 kHz AC voltage frequency at a zero modulation frequency. The extrapolated values were 8.84×10^{14} cm^{-3} and -4.71×10^{17} cm^{-3} for the change in the electron and heavy particle densities, respectively. These were the values used in the aero-optic OPD estimation.

For the aero-optic OPD estimation, a plasma length like that in the experiment of $L = 2.54$ cm was considered. Based on Equations 5 and 7, the electron contribution to the PAO optical phase shift is given as

$$\Phi_e = \frac{-Lq^2\lambda\Delta n_e}{4\pi\epsilon_0 c^2 m}. \tag{11}$$

Similarly, the contribution of the heavy particles to the PAO optical phase shift is given as

$$\Phi_h = \left(A + \frac{B}{\lambda^2}\right)\frac{2\pi L}{\lambda\, n_{h0}}\Delta n_h. \tag{12}$$

Note that in determining the phase shift, Equations 11 and 12 have been divided by a factor of two in order to estimate the optical effect for a *single* pass through the PAO, whereas the interferometer setup used in the experiments featured a double pass through the PAO.

The subsequent contributions of the electron and heavy particle densities to the OPD were then respectively determined using

$$OPD_e = \Phi_e \cdot \frac{\lambda}{2\pi} = \frac{-Lq^2\lambda^2\Delta n_e}{8\pi^2\epsilon_0 c^2 m} \tag{13}$$

and

$$OPD_h = \Phi_h \cdot \frac{\lambda}{2\pi} = \left(A + \frac{B}{\lambda^2}\right)\frac{L\ \Delta n_h.}{n_{h0}}. \tag{14}$$

The values used to evaluate Equations 13 and 14 are given in Table 2. Given the conditions used in the experiment, a total $OPD = -300.8$ nm is predicted, of which the contributions from electron and heavy particles are $OPD_e = -20.14$ nm and $OPD_h = -280.6$ nm, respectively. The predicted total OPD is a factor of two larger than the nominal OPD values in aero-optic applications[2]. However the contribution of the heavy particles is large, which leads to concern about meeting the frequency response goals that exceed current deformable mirrors for OPD control.

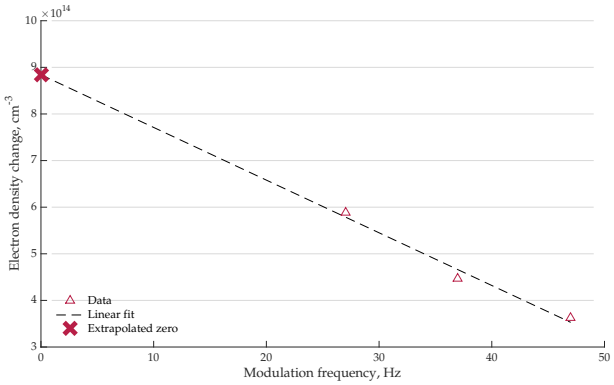

Fig. 17 Electron density as a function of the AC amplitude modulation frequency for an air pressure of 60 Torr and an AC voltage frequency of 4 kHz that was used to extrapolate to zero modulation frequency and denoted by the X-symbol.

V. Summary and Conclusions

The research was the third part of a program to investigate the possibility of using low-temperature ionized air (plasma) for adaptive optics in an airborne laser directed energy system. It involved a novel optical measurement method that consisted of a dual wavelength Michaelson interferometer that included a micro-actuated mirror to allow heterodyne operation. The heterodyne

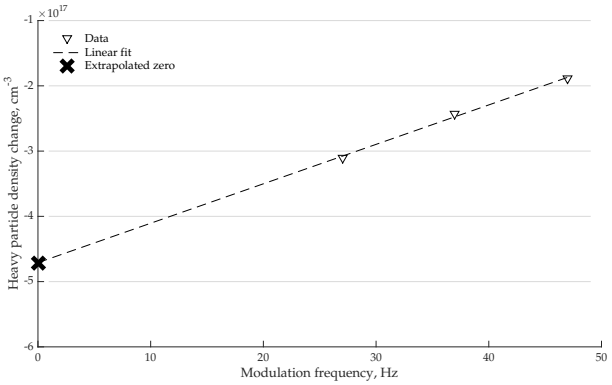

Fig. 18 Heavy particle density as a function of the AC amplitude modulation frequency for an air pressure of 60 Torr and an AC voltage frequency of 4 kHz that was used to extrapolate to zero modulation frequency and denoted by the X-symbol.

Table 2 Parameters used in aero-optic estimation.

Parameter	Variable	Value	Unit
Plasma length	L	0.0254	m
Electron charge	q	1.602×10^{-19}	C
Probing wavelength	λ	10^{-6}	m
Free space permittivity	ϵ_0	8.854×10^{-12}	$A^2\ s^4\ kg^{-1}\ m^{-3}$
Speed of light	c	2.998×10^{8}	$m\ s^{-1}$
Electron mass	m	9.109×10^{-31}	kg
Gas constant for air	A	2.871×10^{-4}	
Gas constant for air	B	1.63×10^{-18}	m^2
Reference heavy particle density	n_{h0}	2.462×10^{25}	m^{-3}
Extrapolated electron density	Δn_e	8.84×10^{20}	m^{-3}
Extrapolated heavy density	Δn_e	-4.71×10^{23}	m^{-3}

interferometry was an important element in extracting the individual effects of electrons and heavy particles on the optical properties of the plasma.

Following our previous design, the plasma was generated in a hollow glass cylinder that was sealed at both ends by optical glass. Electrode bands encircled the outside of the glass cylinder. The electrodes were connected to a high-voltage AC source resulting in a classic double-dielectric

discharge plasma inside the cylinder. The amplitude of the AC source was amplitude modulated in order to produce sideband modulations used for heterodyne analysis. The ratio of the axial distance between the electrode bands to the cylinder inside diameter conformed to our previously determined critical value for the plasma to form along the axial centerline of the hollow cylinder[9].

The plasma adaptive optic (PAO) element was located in one arm of the heterodyne interferometer. The time evolution of interferometric fringes produced by the PAO were acquired. A robust demodulation scheme was developed to extract the modulated interferometric phase shifts to reveal the temporal evolution of electron and heavy particle densities within the PAO. The data documented a number of important trends. The first was that the magnitude of the change (plasma on minus plasma off) in the electron density was three-orders of magnitude smaller than that for the heavy particles. The $\mathcal{O}(10^{14})$ cm^{-3} change in electron density was consistent with the diffusive nature of the PAO plasma, and the power levels supplied. The electron density increased with increasing PAO air pressure which was consistent with a decreasing air mean-free-path at higher pressures. The electron density also increased with the AC voltage frequency which correlated with the higher AC power supplied per amplitude modulation cycle. For a constant AC frequency, the electron density decreased with increasing AC amplitude modulation frequency. The trend with the heavy particle density was always opposite to that of the electron density. That is it decreased with increasing air pressure and AC voltage frequency, and increased with increasing AC amplitude modulation frequency.

In all of the cases, the majority of the observed changes in heavy particle and electron densities was associated with the dynamics of the plasma amplitude modulation. With regard to one case with the highest AC frequency and air pressure condition, a small decrease in the heavy particle density at the end of the amplitude modulation cycle could be the consistant with a small increase in the mean temperature of the air. However, that difference was small compared to the peak change in the heavy particle density which was ultimately used to evaluate the effectiveness of the PAO.

The experimental results of the change in electron and heavy particle densities were used to determine the PAO OPD for the aero-optic standard probing wavelength of 1 μm. This involved experimental conditions that led to the highest electron densities, namely the highest air pressure of

60 Torr and the highest AC voltage frequency of 4 kHz. The particle densities were extrapolated to reflect a zero AC amplitude modulation frequency that is representative of the PAO operation. The extrapolated values for the change in the electron and heavy particle densities used in the aero-optic OPD estimation were 8.84×10^{14} cm^{-3} and -4.71×10^{17} cm^{-3}. These resulted in a total OPD of -300.8 nm of which the contributions from electron and heavy particles was $OPD_e = -20.14$ nm and $OPD_h = -280.6$ nm, respectively. The total OPD was a factor of two larger than nominal OPD values in aero-optic applications[2], however the large contribution of the heavy particles causes concern about meeting the frequency response goals to exceed current deformable mirrors for OPD control.

Acknowledgments

This work was supported by a Department of the Navy, Space and Naval Warfare Systems Command (SPAWAR) Award N65236-12-1-1001. The authors are grateful for the support of this technology effort.

[1] Jumper, E. and Fitzgerald, E., "Recent advances in aero-optics," *Progress in Aerospace Sciences*, Vol. 37, No. 3, 2001, pp. 299–339.

[2] Gordeyev, S. and Jumper, E., "Fluid Dynamics and Aero-Optical Environment Around Turrets," *40th AIAA Plasmadynamics and Lasers Conference*, AIAA, Washington, DC, 2009.

[3] Siegenthaler, J., Jumper, E., and Gordeyev, S., "Atmospheric Propagation Vs. Aero-Optics," *46th AIAA Aerospace Sciences Meeting and Exhibit*, AIAA, Reston, VA, 2008.

[4] Mani, A., Wang, M., and Moin, P., "Computational Study of Aero-Optical Distortions by a Turbulent Wake," *Optical Society of America*, Vol. 23, No. 12, 2006, pp. 3027–3035.

[5] Becker, K., Kogelschatz, U., Schoenbach, K., and Barker, R., *Non-Equilibrium Air Plasmas at Atmospheric Pressure*, Institute of Physics Publishing, Philadelphia, PA, 2005.

[6] Uhm, H., Yoo, N., and Choi, E., "Influence of Plasma Decay on Emission of 147-nm Ultraviolet Light from Discharge Cells in the Plasma Display Panel," *Physics of Plasma*, Vol. 14, 2007.

[7] Neiswander, B., Matlis, E., and Corke, T., "Plasma Lens for Optical Path Difference Control," *AIAA*, Vol. 50, No. 1, 2012, pp. 123–130.

[8] Hutchinson, I. H., *Principles of Plasma Diagnostics*, Cambridge University Press, 2nd ed., 2002, Cambridge Books Online.

[9] Neiswander, B., Matlis, E., and Corke, T., "Geometric Optimization of a Cylindrical Plasma Adaptive Optics Lens," *AIAA*, Vol. 51, No. 3, 2013, pp. 657–664.

[10] Duschin, L. and Pawlitschenko, O., *Plasmadiagnostik mit Lasern*, Akademie-Verlag, Berlin, 1973.

[11] Feynman, R., Leighton, R., and Sands, M., *The Feynman Lectures on Physics*, Vol. II, Addison-Wesley Publishing Company, Inc., Nov. 1964.

[12] Leipold, F., Stark, R., and El-Habachi, A., "Electron Density Measurements in an Atmospheric Pressure Air Plasma by Means of Infrared Heterodyne Interferometry," *Journal of Physics D: Applied Physics*, Jan. 2000.

[13] Urabe, K., Choi, J., Ito, Y., Tachibana, K., and Sakai, O., "Diagnostics of Dielectric Barrier Discharge at Atmospheric Pressure by Laser Spectroscopic Measurements," *Proc. 19th Int. Symp. on Plasma Chemistry (Bochum, Germany)*, 2009.

[14] Alpher, R. and White, D., "Interferometric measurement of electron concentrations in plasmas," *Physics of Fluids*, Vol. 1, No. 5, 1958, pp. 452–453.

[15] Schoenbach, K., "Basic studied of high pressure air plasmas," Report 20061016145, AFOSR, 2005.

[16] Baker, D. and Lee, S.-T., "Dual laser interferometer for plasma density measurements on large tokomaks," *Rev. Sci. Instrum.*, Vol. 49, No. 12, 1978, pp. 919–922.

[17] Wolfe, S., Button, K., Waldman, J., and Cohn, D., "Modulated submillimeter laser interferometer system for plasma density measurements." *Applied Optics*, Vol. 15, No. 11, 1976, pp. 2545–2648.